7-15-2020

Portable, field-based neuroimaging using high-density diffuse optical tomography

Andrew K. Fishell

Ana María Arbeláez

Claudia P. Valdés

Tracy N. Burns-Yocum

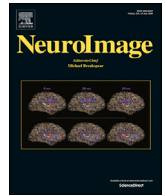Arefeh Sherafati

See next page for additional authors

Authors

Andrew K. Fishell, Ana María Arbeláez, Claudia P. Valdés, Tracy N. Burns-Yocum, Arefeh Sherafati, Edward J. Richter, Margarita Torres, Adam T. Eggebrecht, Christopher D. Smyser, and Joseph P. Culver

Portable, field-based neuroimaging using high-density diffuse optical tomography

Andrew K. Fishell [a,b], Ana María Arbeláez [c], Claudia P. Valdés [d], Tracy M. Burns-Yocum [e],
Arefeh Sherafati [a,f], Edward J. Richter [g], Margarita Torres [d], Adam T. Eggebrecht [b,c],
Christopher D. Smyser [b,c,h], Joseph P. Culver [a,b,f,i,*]

[a] Washington University School of Medicine, Division of Biology and Biomedical Sciences, St. Louis, MO, USA
[b] Washington University School of Medicine, Mallinckrodt Institute of Radiology, St. Louis, MO, USA
[c] Washington University School of Medicine, Department of Pediatrics, St. Louis, MO, USA
[d] Centro Médico Imbanaco, Cali, Valle del Cauca, Colombia
[e] Indiana University, Department of Psychological and Brain Sciences, Bloomington, IN, USA
[f] Washington University, Department of Physics, St. Louis, MO, USA
[g] Washington University, Electrical and Systems Engineering, St. Louis, MO, USA
[h] Washington University School of Medicine, Department of Neurology, St. Louis, MO, USA
[i] Washington University, Department of Biomedical Engineering, MO, St. Louis, USA

ARTICLE INFO

ABSTRACT

Behavioral and cognitive tests in individuals who were malnourished as children have revealed malnutrition-related deficits that persist throughout the lifespan. These findings have motivated recent neuroimaging investigations that use highly portable functional near-infrared spectroscopy (fNIRS) instruments to meet the demands of brain imaging experiments in low-resource environments and enable longitudinal investigations of brain function in the context of long-term malnutrition. However, recent studies in healthy subjects have demonstrated that high-density diffuse optical tomography (HD-DOT) can significantly improve image quality over that obtained with sparse fNIRS imaging arrays. In studies of both task activations and resting state functional connectivity, HD-DOT is beginning to approach the data quality of fMRI for superficial cortical regions. In this work, we developed a customized HD-DOT system for use in malnutrition studies in Cali, Colombia. Our results evaluate the performance of the HD-DOT instrument for assessing brain function in a cohort of malnourished children. In addition to demonstrating portability and wearability, we show the HD-DOT instrument's sensitivity to distributed brain responses using a sensory processing task and measurements of homotopic functional connectivity. Task-evoked responses to the passive word listening task produce activations localized to bilateral superior temporal gyrus, replicating previously published work using this paradigm. Evaluating this localization performance across sparse and dense reconstruction schemes indicates that greater localization consistency is associated with a dense array of overlapping optical measurements. These results provide a foundation for additional avenues of investigation, including identifying and characterizing a child's individual malnutrition burden and eventually contributing to intervention development.

1. Introduction

Despite increased efforts focused upon reducing the prevalence of childhood malnutrition and the high mortality rates associated with this condition, its deleterious effects on brain development remain a pressing global health concern (Goyal et al., 2014; Kuzawa et al., 2014; Chugani et al., 1987; Thompson and Nelson, 2001). During the first decade of life,

the human brain has exceptional nutritional and metabolic requirements as the brain undergoes critical structural and functional changes, including neuronal development, synaptogenesis, and synaptic remodeling (Thompson and Nelson, 2001; Goyal and Raichle, 2013; Wiggins, 1982; Murthy and Desiraju, 1991). Thus, if nutrients are scarce and energetic demands are unmet during this critical period, trajectories of brain development can be irreversibly compromised, leading to

life-altering deficits (Black et al., 2019; Liu et al., 2003; Grantham-Mc-Gregor et al., 2007). Correlational studies of growth during early childhood underscore the importance of proper nutrition during development, as a child's weight gain during the first two years of life is related to subsequent performance in school (Martorell, 1999; Martorell et al., 2010). Additional studies show a relationship between malnutrition status and attainment of WHO-established motor milestones, social behaviors, and linguistic abilities (Iannotti et al., 2016; Barrett et al., 1982). Interventional studies have also directly assessed the effect of various therapeutic feeding regimens and supplements on subsequent neurodevelopmental outcomes, establishing a causal link between childhood malnutrition and brain development (Grantham-McGregor et al., 1991; Cusick and Georgieff, 2012; McKay et al., 1978). If malnutrition is unaddressed during childhood, its long-term sequelae include psychiatric, cognitive, behavioral, and social deficits that persist throughout the lifespan (Liu et al., 2003; Prado and Dewey, 2014; Waber et al., 2011). In turn, these lifelong consequences may impact social and economic development on a global and/or national scale (Hoddinott et al., 2008).

Malnutrition-related deficits revealed using behavioral assessments have raised additional questions regarding the neurological changes underlying behavioral differences between typically developing and malnourished children (Nelson, 2015; Raizada and Kishiyama, 2010). Assessing compromised brain development in regions where malnutrition is highly prevalent requires careful selection of methods that are both sensitive to a child's malnutrition burden and practical to implement in low-resource settings. Widely used neuroimaging modalities, such as magnetic resonance imaging (MRI), can elucidate typical and atypical developmental trajectories, but are often poorly suited for global neuroimaging contexts due to the limited portability, need for specialized facilities, and the high cost associated with these methods (JL and R, 2082; Smyser et al., 2010; Estep et al., 2014; Smyser et al., 2011; Smyser et al., 2013; Greene et al., 2016). To address the need for neuroimaging studies in these environments, researchers have increasingly turned to more portable electrical neuromonitoring and optical neuroimaging instrumentation. These portable tools, including electroencephalography (EEG) (Jensen et al., 2019), functional near-infrared spectroscopy (fNIRS) (Lloyd-Fox et al., 2014, 2016; Lloyd-Fox et al., 2019), and diffuse correlation spectroscopy (DCS) (Roberts et al., 2017), effectively create mobile neuroimaging laboratories that can be deployed virtually anywhere, eliminating practical constraints imposed by costly and immobile neuroimaging facilities.

These mobile neuroimaging methods have begun to address the urgent need for portable and inexpensive tools for assessing brain function in low-resource settings. In addition to establishing these methods in new regions where neuroimaging research may be unfamiliar, investigators using these highly portable techniques must also achieve results demonstrating high-quality data and risk sensitivity in the population(s) of interest. To date, research based in The Gambia, Guinea-Bissau, and Bangladesh supports the feasibility for using these tools to perform field-based brain imaging experiments, and recent results show altered cortical physiology related to early adversity and malnutrition (Jensen et al., 2019; Lloyd-Fox et al., 2016; Roberts et al., 2017). However, these studies have been limited by the relatively low channel counts and sparse imaging arrays.

High-density diffuse optical tomography (HD-DOT) is an optical neuroimaging modality that, like fNIRS, uses near-infrared light to measure tissue oxygenation, resulting in a hemodynamic measure of neuronal activity, similar to techniques such as fMRI. However, unlike fNIRS, HD-DOT utilizes a densely overlapping measurement array, which produces tomographic images of cortical hemodynamics with consistent and stable point-spread functions that approach the resolution of common multi-subject fMRI studies (Eggebrecht et al., 2012, 2014). While HD-DOT has successfully mapped distributed brain function using both task-evoked responses and resting-state functional connectivity in healthy adults, adults with Parkinson's, and infants in the Neonatal Intensive Care Unit, it has not yet been established for applications

demanding highly mobile instruments, or on-site studies of childhood malnutrition (Eggebrecht et al., 2014; Ferradal et al., 2016; White and Culver, 2010a, 2010b).

The goal of this work is to evaluate the performance of a field-optimized HD-DOT system in the context of malnutrition. We used both task-evoked responses and functional connectivity measures to establish feasibility of imaging chronically malnourished children recruited as part of a larger study investigating the effects of malnutrition on brain development and cognition in Cali, Colombia. Task-evoked responses to a passive auditory processing task were used to evaluate response localization performance and data quality in this novel cohort. Assessment of homotopic functional connectivity was used to evaluate sensitivity to distributed brain function, setting the stage for future assessments of malnutrition burden across multiple cortical systems, using this powerfully predictive imaging paradigm (Wheelock et al., 2018). Our results demonstrate that HD-DOT with both high channel count and high-density imaging arrays can be preserved in a portable, field-ready optical neuroimaging system and can confer the image quality and localization improvements associated with tomographically reconstructed images of brain function in a non-laboratory setting.

2. Methods

2.1. Participants

Participants in this experiment were recruited from the urban and peri-urban regions surrounding Cali, Colombia. Families were primarily recruited from community health and educational programs established by the Cali Department of Health, the Malnutrition Rehabilitation Program for the municipality, and some school lunch programs. In accordance with experimental protocols approved by the Human Research Protection Offices at Washington University and the Centro Medico Imbanaco Ethics Committee, caregivers gave written consent and participants gave verbal assent to participate in the study. All participants had normal physical examinations and were not acutely ill at the time of study. No participants had a personal history of premature birth, diabetes, chronic disease, psychiatric, or neurological conditions. In total, a cohort of 30 participants were enrolled in the HD-DOT experiments. Participants were excluded primarily due to poor cap fit, excessive motion, or failure to complete the entire imaging protocol (N = 13), leaving a total of 17 participants (Mean age = 8.4 years, SD = 0.9 years; 9 females, 8 males) in the subsequent analyses (Table 1). The frequency of success increased as experience was gained within the experimental team at Cali. The data and analysis tools used in this study are available upon reasonable request to the corresponding author.

2.2. Experimental procedures and stimuli

Participants underwent an HD-DOT cap fit procedure lasting approximately 5–10 min. Cap fit was optimized for a given participant using real-time displays of measurement light level, optode signal-to-

Table 1
Demographics.

N	17		
Sex	8 male; 9 female		
	Mean	**SD**	**Range**
Age (years)	8.4	0.9	7–10
Head Circumference (cm)	51.4	1.7	49–54.4
Height (cm)	128	6.0	118.5–140
Weight (kg)	24.2	4.7	18.2–33
Height-for-Age (WHO Z-Score)	−0.5	1.1	−2.44–1.31
Weight-for-Age (WHO Z-Score)	−0.9	1.2	−3.64–0.95

Demographic information for participants included in HD-DOT analyses.

noise, and optode-scalp coupling coefficients. This procedure ensured that the greatest possible number of optical measurements would be retained for subsequent analysis. During cap fit, hair was combed and secured such that it did not obscure optodes, and the cap was secured to the participant's head using hook-and-loop straps on the forehead and chin to ensure consistent placement. Following cap fit, participants completed two experimental paradigms: passive word listening and passive movie viewing. Participants alternated between the two paradigms until three repetitions of each paradigm were acquired or the experimenter judged that the participant began to move excessively or became too fatigued to continue with the experiment. All stimuli were presented using a liquid crystal display monitor positioned at eye-level approximately 90 cm in front of the seated participant, as well as a speaker positioned in front of the participant.

2.2.1. Passive word listening

In order to fully compare results from the present HD-DOT instrument with prior work, the passive word listening paradigm was presented in a block design, specifically following previously published HD-DOT procedures (Eggebrecht et al., 2014). Possible systemic physiology that might be entrained to the stimulus was removed using a combination of superficial signal regression and tomographic reconstruction techniques, the effectiveness which has been previously detailed (Eggebrecht et al., 2014; Gregg et al., 2010; Zeff et al., 2007). During the passive word listening task, participants listened to lists of spoken Spanish concrete nouns in a block design. Words were presented at a rate of 1 word/second for 15 s, followed by 15 s of silence. During a single 3-min run, participants listened to 6 blocks of words (90 words in total). The passive word listening task was chosen because it has been previously published with both fMRI and HD-DOT (Eggebrecht et al., 2014), producing reliable activations to a sensory stimulus. Further, this task was not hypothesized to show any malnutrition- or age-related effects, underscoring that this task was intended to generate activation maps consistent with previous studies (Eggebrecht et al., 2014), enabling assessment of data quality, image reconstruction procedures, instrument performance, and localization capabilities.

2.2.2. Passive movie viewing

During a passive movie viewing run, participants were instructed to sit still and quietly watch an unedited, continuous 10-min segment from *Buscando a Nemo* (*Finding Nemo*). Participants viewed one of two clips, lasting from either (00:45–10:45) or (10:45–20:45). The passive movie
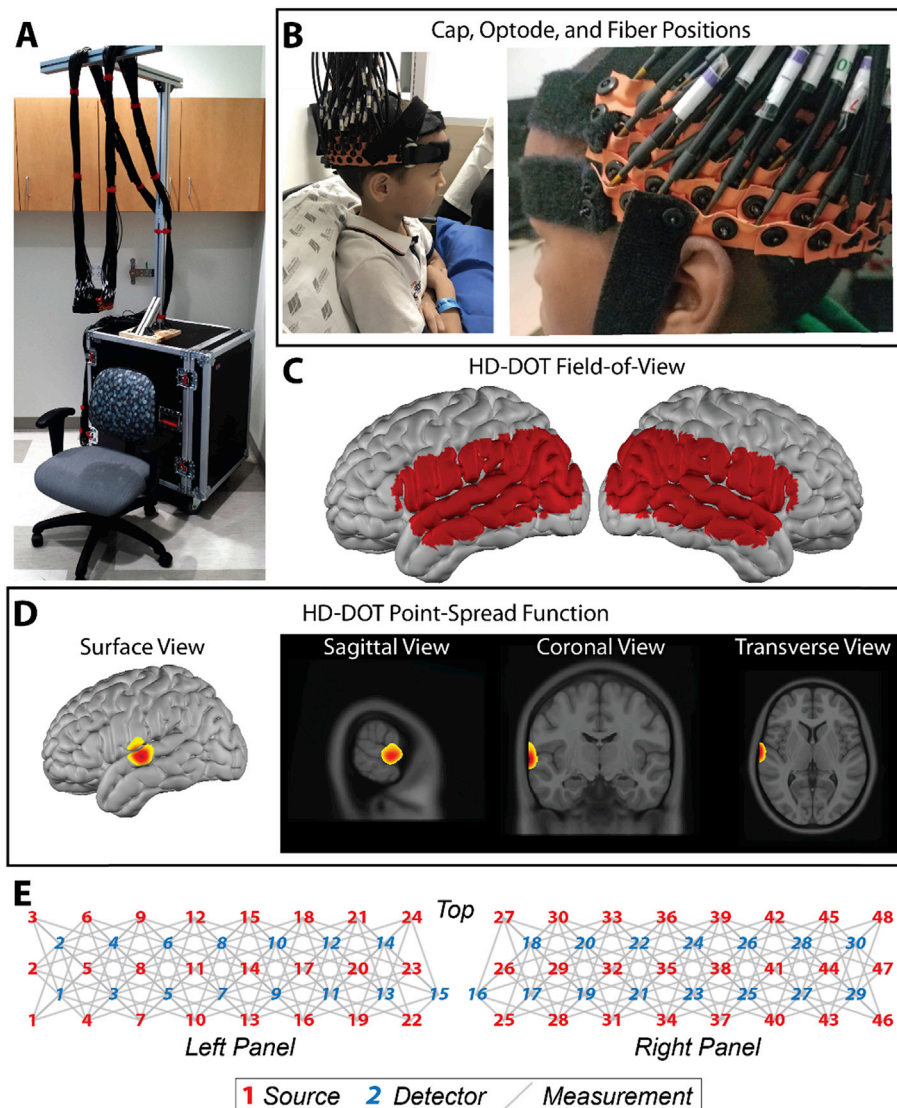

Fig. 1. HD-DOT Instrumentation.
A: The HD-DOT instrument used in these experiments is a portable, self-contained instrument containing all opto-electronic equipment needed for the 30 detector by 48 source system. The instrument includes a removable fiber support system, ensuring that the participant's head bears no weight from the fibers. The overall footprint for this system is 76 × 55 cm. **B:** HD-DOT cap position on two participants in Cali, Colombia. **C:** The field-of-view based on optode positions, projected on to the surface of the MNI atlas. **D:** Simulated point-spread function for the HD-DOT system, shown on the cortical surface and volumetric slices of the MNI atlas. **E:** Optode layout for both panels of the HD-DOT cap, including sources (red numbers), detectors (blue numbers), and first through third nearest-neighbor measurements (grey lines).

viewing task was chosen because it enabled acquisition of a continuous, 10-min measurement of brain activity, permitting analysis of functional connectivity, which can be related to outcomes in pediatric populations (Wheelock et al., 2018). Critically, in pediatric populations, functional connectivity measured during periods of quiet fixation resulted in greater head movement relative to functional connectivity assessed during movie viewing (Greene et al., 2018; Vanderwal et al., 2015). Therefore, passive movie viewing was chosen in order to maximize both the number of useable low-motion time points within a dataset and total useable functional connectivity datasets.

2.3. High-density diffuse optical tomography instrumentation

2.3.1. Design specifications

The HD-DOT instrument built for field use in these experiments (Fig. 1) followed design specifications for previously published HD-DOT instruments (Eggebrecht et al., 2012, 2014), but was optimized to have a smaller footprint (W = 24.25 in x D = 22.75 in x H = 33 in) in a single self-contained console, in order to maximize portability and usability. The instrument used in this work was a custom-built continuous wave instrument, consisting of 48 LED sources illuminating the head at two wavelengths (λ = 750 nm and 850 nm), and 30 avalanche photodiodes (Hamamatsu C5460-01), coupled to the head using fiber-optic bundles (2.5-mm diameter bundles of 50 μm fibers).

The weight of the 78 fibers was managed using a custom-built, collapsible support made of extruded aluminum, ensuring that the participant's head did not bear any weight from the fibers. Fiber tips were positioned on the scalp using a custom-built neoprene imaging cap, which maintained an optode geometry such that first-through third-nearest neighbor separations were 13, 29, and 39 mm, respectively. Temporal, frequency, and spatial encoding of the source illumination pattern achieved an overall HD-DOT framerate of 10 Hz. As in other optical neuroimaging systems, a measurement consists of the light level between a single source-detector pair. The total number of first-through third-nearest neighbor measurements afforded by this array configuration was 324 measurements per wavelength (116 first nearest neighbor, 158 s nearest neighbor, 50 third nearest neighbor). These measurements were converted into volumetric, voxelated movies of brain hemodynamics using the image reconstruction procedures described in Section 2.4.

2.3.2. Instrument setup

Critical considerations for imaging instruments used in non-laboratory settings include factors such as portability, quick setup, and ease of use, which are not necessarily considerations for fixed instruments that remain in laboratory environments. The large channel count on the field HD-DOT system used in this work necessitated a design that facilitated imaging by a variety of users. Consequently, the instrument was designed to be encased in a commercially available equipment cart (Gator G-TOUR16UCA-24D), which had a footprint of 22.75 × 24.25 in. This design enabled the HD-DOT instrument to be readily transported and positioned at the imaging site at Centro Medico Imbanaco. Of note, the HD-DOT instrument was ready for imaging after 4 h of setup on site and training new HD-DOT users was complete after 5 working days of guided imaging, highlighting the ease of use associated with this HD-DOT instrument.

2.4. Image reconstruction

2.4.1. Measurement pre-processing and anatomical light modeling

As previously published using existing HD-DOT systems, image reconstruction occurs in five steps: light-level measurement pre-processing, anatomical light modeling, image reconstruction, spectroscopy, and spatial normalization (Eggebrecht et al., 2014). To begin, raw detector light levels were converted to a time-series of log-ratio data, using the temporal mean of a given measurement as its baseline. An

initial quality control step identified measurements with excessive noise by excluding any measurement with a temporal standard deviation exceeding 7.5%, as this excessive variance was more likely to reflect nuisance variance (e.g. head motion) than it was to reflect variance related to cortical hemodynamics. To facilitate comparisons with previous studies in St. Louis, the measurement variance threshold applied was held constant with previous HD-DOT work (Eggebrecht et al., 2014). Future work should examine these and other reconstruction parameters comprehensively. Subsequently, the measurements that passed the variance threshold were then high-pass filtered (passive word listening cutoff: $f_{hpc} > 0.02$ Hz; passive movie viewing cutoff: $f_{hpc} > 0.009$ Hz). Next, nuisance signals resulting from systemic or superficial (i.e. scalp and skull) physiology were approximated using the average of all first nearest neighbor measurements, whose spatial sampling is most superficial in the tissue. This superficial signal was regressed out of all measurements. Finally, the measurements were low-pass filtered (passive word listening cutoff: $f_{lpc} < 0.5$ Hz; passive movie viewing cutoff: $f_{lpc} < 0.08$ Hz).

Anatomical light modeling requires either a subject-specific or an atlas-based segmented anatomy. In these experiments, an age appropriate atlas-based model was used, in order to eliminate the need for subject-specific anatomy obtained with costlier and frequently unavailable modalities such as MRI or CT. Atlas-based forward modeling has been previously shown to result in reasonable individual and group-level localization errors on the order of millimeters (Ferradal et al., 2014). A non-linear ICBM152 atlas from the Montreal Neurological Institute was used for image reconstruction in this work (Fonov et al., 2011; Mazziotta et al., 2001). This atlas is segmented into five tissue compartments in order to account for the unique optical properties of each: scalp ($\mu_{a,750} = 0.017$; $\mu_{a,850} = 0.019$; $\mu_{s,750}' = 0.74$; $\mu_{s,850}' = 0.64$), skull ($\mu_{a,750} = 0.012$; $\mu_{a,850} = 0.014$; $\mu_{s,750}' = 0.94$; $\mu_{s,850}' = 0.84$), grey matter ($\mu_{a,750} = 0.018$; $\mu_{a,850} = 0.019$; $\mu_{s,750}' = 0.84$; $\mu_{s,850}' = 0.67$), white matter ($\mu_{a,750} = 0.018$; $\mu_{a,850} = 0.021$; $\mu_{s,750}' = 1.19$; $\mu_{s,850}' = 1.01$), and cerebrospinal fluid ($\mu_{a,750} = 0.004$; $\mu_{a,850} = 0.004$; $\mu_{s,750}' = 0.3$; $\mu_{s,850}' = 0.3$) (Eggebrecht et al., 2012; Bevilacqua et al., 1999; Custo et al., 2006; Strangman et al., 2002). Next, the atlas anatomy was computed from the segmented atlas and combined with the grid of the 30 detector and 48 source optodes, which was positioned using cranial landmarks and relaxed on to the mesh using a spring-relaxation energy minimization algorithm following previously published methods (Joseph et al., 2006). Using this mesh, a sensitivity matrix was generated using NIRFAST (Dehghani et al., 2008) for each wavelength. The sensitivity matrix was subsequently inverted using Tikhonov regularization, and spectroscopy was performed using literature-derived values (Eggebrecht et al., 2012; Bluestone et al., 2001).

The output of the image reconstruction procedure was volumetric time-series data, down-sampled from 10 Hz to 1 Hz for three hemoglobin contrasts: oxyhemoglobin (ΔHbO_2), deoxyhemoglobin (ΔHbR) and total hemoglobin (ΔHbT). All analyses performed on these images utilize the oxyhemoglobin (ΔHbO_2) contrast, unless otherwise specified.

2.4.2. Head motion quantification

To quantify the amount of head motion present during an imaging run, we leveraged the inherent covariance induced by head motion across optical measurements. The temporal variance across measurements y was quantified using the Global Variance in the Temporal Derivative (GVTD) (Sherafati et al., 2017). For a given run, GVTD was computed over a matrix with n measurements and T timepoints. The squared temporal derivative for a given timepoint i and measurement j, (y_{ji} - $y_{j(i-1)}$) (Kuzawa et al., 2014), was then computed. Finally, to generate a single timeseries quantifying GVTD over the course of the run, the root mean square was taken over the temporal derivative of all measurements, such that GVTD, g, for timepoint i, $g_i = \sum_{j=1}^{n} \frac{1}{n} \sqrt{(y_{ji} - y_{j(i-1)})^2}$, where n is

the total number of measurements. This metric is analogous to the DVARS metric used to assess head motion in fMRI datasets (Smyser et al., 2010), and enables comparison of head motion related variance across data collected across sites, instruments, and cohorts.

2.5. Image analysis

2.5.1. Passive word listening

The passive word listening task delivered auditory stimulation in a block design, with alternating blocks of stimulation ("On") and no stimulation ("Off"). Consequently, the magnitude of the cortical response to the stimulus was calculated by comparing the voxel-wise responses during the On and Off conditions. During each 30-s block, the stimulus was on for 15 s, followed by 15 s of silence. All blocks from a single participant were then averaged to produce a single volumetric movie containing the block-averaged response to the stimulus. The difference between voxelwise responses during the On and Off conditions was estimated by averaging seconds 10–19 of the block ("On") and contrasting that response to seconds 20–29 of the block ("Off"). A random effects t-statistic was computed across participants to assess the magnitude of the contrast between conditions.

2.5.2. Passive movie viewing

Hemoglobin timeseries obtained during passive movie viewing were filtered to the functional connectivity band $(0.009 < f < 0.08)$ in order to examine patterns of hemoglobin fluctuation representing correlated, or functionally connected, brain regions (Vanderwal et al., 2018). As in previous work using HD-DOT to measure functional connectivity, a seed-based approach was used to assess patterns of homotopic, or bilateral, connectivity (Ferradal et al., 2016). Seeds consisted of 12 spheres (radius $5 = mm$) placed across the HD-DOT field-of-view. For each seed, functional connectivity was computed by averaging the ΔHbO_2 signal for all voxels within the sphere, to generate a single time-series for the seed. This time-series was then cross-correlated with every other seed to produce a correlation matrix showing the functional connectivity between pairs of seed regions. To assess functional connectivity between a single seed and all voxels within the field-of-view, a spatial map of Pearson product-moment correlations was generated by cross correlating the seed ΔHbO_2 timeseries with the voxelwise ΔHbO_2 timecourses from across the entire field-of-view. Individual correlation maps were then converted to a normally distributed statistic using the Fisher's z-transformation. Finally, group-average connectivity maps were generated by averaging individual z-transformed seed maps across all subjects.

2.6. Sparse array reconstruction and analysis

The HD-DOT measurement array results in a densely overlapping set of measurements, which produces depth-resolved images of brain function with a point-spread function comparable to images obtained with fMRI. However, sparser measurement arrays are often favored over dense arrays due to the reduced channel count, which results in a smaller instrument with fewer fibers affixed to the participant's head. We evaluated the effect of measurement density by reconstructing passive word listening data using a sparse array. A sparse array was constructed by selecting a subset of second nearest neighbor measurements from the larger set of HD-DOT measurements to achieve a measurement count comparable with other fNIRS systems used for global health applications (Lloyd-Fox et al., 2014). These sparse array measurements were selected to have the same lateral coverage as the HD-DOT array, but with no overlapping source-detector measurements. The resulting simulated sparse array consisted of 16 measurements per hemisphere, for a total of 32 measurements at a 29-mm separation (compared to the total of 324 measurements for HD-DOT).

Measurement processing, image reconstruction, and image analysis followed the same procedures outlined in Sections 2.4.1 and 2.5.1, with

one notable exception. Because the sparse measurement array did not contain any measurement pairs with a short source-detector separation, no superficial signal regression was performed further on the measurement set (Gregg et al., 2010). Without measurements with a short source-detector separation, the superficial nuisance signal is not readily approximated.

Spatial overlap maps were used to quantify the agreement between passive word listening activations reconstructed using the dense and sparse reconstruction schemes, leveraging the reliability of the activations produced by the passive word listening paradigm. Spatial overlap between sparsely and densely reconstructed images was computed at the single-subject level. First, the single-subject maps were thresholded. The threshold for each map was set at 25% of the maximum voxel value for that map. A map-specific threshold was chosen to account for differences in activation magnitude from the sparse and dense reconstructions. Following thresholding, maps were then binarized, such that any voxel surviving the threshold was set to 1, and all remaining voxels were set to 0. Next, to evaluate the activation overlap for the dense maps, all binarized maps were summed. In the resulting image, the voxel value indicates the number of participants with an overlapping activation in that voxel. The same summing procedure was repeated for the sparse maps, in order to similarly quantify the number of participants with spatially overlapping activations following image reconstruction with the sparse measurement set.

To compute the spatial overlap between individual activation maps and the group-averaged activation map, individual maps were again thresholded and binarized as described above. The spatial overlap between the dense/sparse activation maps and the respective dense or sparse group-average map was computed by the conjunction between the two binarized images. Summing across individual conjunction images resulted in a map showing the extent to which the dense and sparse reconstruction schemes produced individual passive word listening activations consistent with the group average response.

3. Results

3.1. Wearability and data quality

On average, participants completed an average of 28.5 min (SD = 7 min) of imaging, including two repetitions of the passive word listening task (3-min duration), and two repetitions of the passive movie viewing (10-min duration). Combined with short breaks between imaging runs and 5–10 min for initial cap fit, participants in this study wore the HD-DOT cap for approximately 33.5–38.5 min per session, depending on the exact cap fit duration. The session durations indicate the tolerability of HD-DOT imaging in this cohort of 7-9-year-old children with no prior experience participating in brain imaging experiments.

Scan duration provided an indicator for participant comfort and instrument ergonomics. In addition, we assessed measurement data quality using a battery of readouts generated during image reconstruction (Fig. 2). These readouts ensure that only high-quality measurements are used in reconstruction, mitigating the deleterious effects of including measurements contaminated by poor optode-scalp coupling or head motion. As shown in Fig. 2, HD-DOT measurements are of sufficient quality across the entire field-of-view, resulting in cortical coverage at three source-detector separations. Finally, signal-to-noise at the participant's pulse frequency (Fig. 2, E) verified that measurements were sensitive to vascular physiology. These quality control procedures aid the reconstructed steps to yield high-fidelity imaging of brain function.

Measurement retention as a function of source-detector separation was relatively consistent across the cohort (Supplemental Fig. 1), with an average of 94% of first nearest-neighbor measurements, 77% of second nearest-neighbor measurements, and 24% of third nearest-neighbor measurements retained per participant. Further, using GVTD, as described in Section 2.4.2, to quantify head-motion induced variance in
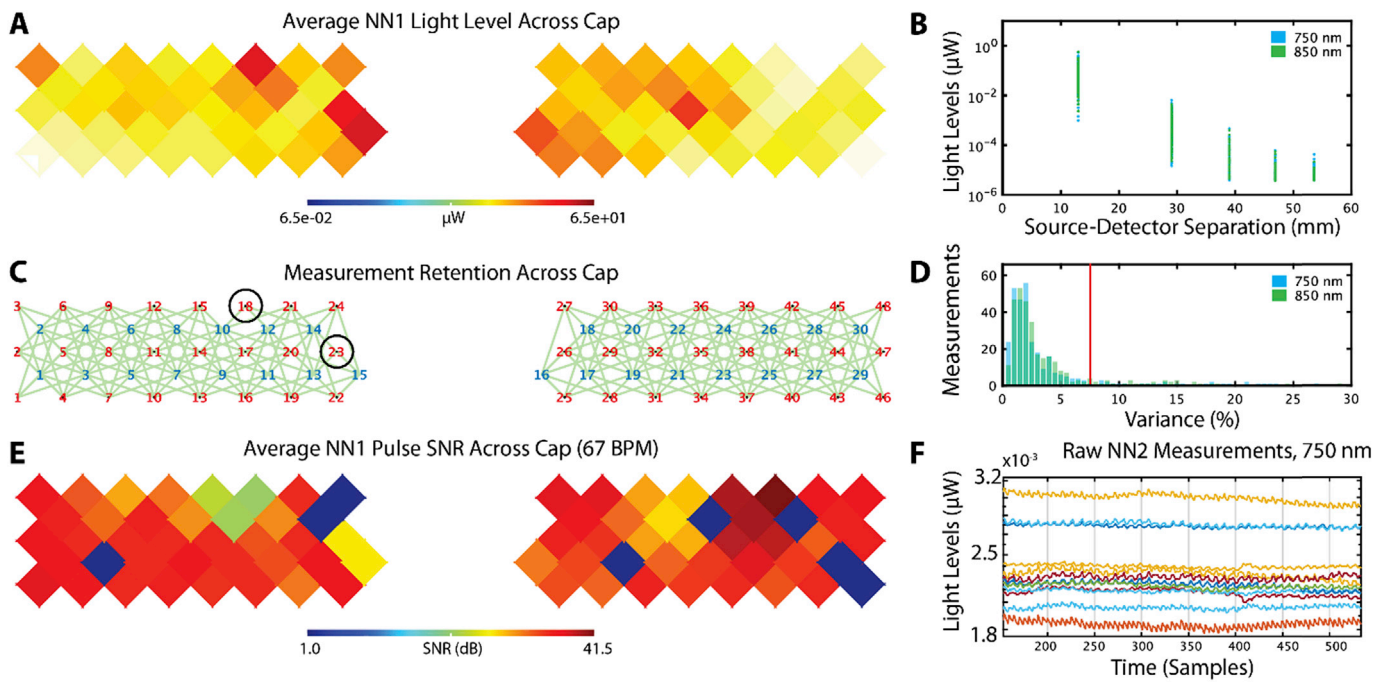
Fig. 2. The data quality report generated during image reconstruction indicates the measurement quality obtained during a single scan and includes multiple measurement quality assessments used to determine the usability of a scan in real-time. This report was generated from a representative subject during a passive word listening acquisition. **A:** The average light level for first nearest neighbor (NN1) measurements across the two panels of the HD-DOT cap indicated relatively strong light levels across the cap. **B:** A plot of light level as a function of source-detector separation (i.e. measurement distance) showed log-linear light falloff, as would be expected in biological tissue. **C:** The plot of measurement retention for this acquisition showed measurements retained for subsequent image reconstruction (green lines), as well as optodes where at least 33% of measurements were rejected (black circles). In this cap fit, 232/232 NN1, 295/316 NN2, and 27/100 NN3 measurements were retained. **D:** The histogram of measurement-wise temporal variance indicated that most measurements are below the temporal variance threshold (7.5%, red line) imposed to exclude measurements contaminated by movement or poor optode coupling. **E:** The pulse signal-to-noise for first nearest-neighbor measurements showed, in general, strong signal-to-noise ratio at the participant's pulse frequency, indicating good sensitivity to vascular physiology needed to image cortical hemodynamics. **F:** A plot of individual second nearest-neighbor measurements showed sensitivity to the participant's pulse, and a lack of global variance across measurements that could be associated with global noise introduced by head motion.

each dataset (Supplemental Fig. 2) shows that data quality quantified using this metric is comparable to HD-DOT data quality across multiple sites, instruments, and age groups.

3.2. Task-evoked responses

Group-averaged oxyhemoglobin activation maps from the passive word listening paradigm are displayed in Fig. 3. This group average map contains activation data from 17 individual participants, who in total completed 64 runs of the passive word listening task. The group average map (Fig. 3, A) reveals elevated oxyhemoglobin concentration in bilateral superior temporal gyrus, the same cortical region activated by this task in prior work (Eggebrecht et al., 2014). Further, the time course of the hemodynamic response (Fig. 3, B) shows the expected elevation in oxyhemoglobin concentration followed by return to baseline.

We used a t-statistic to contrast the voxelwise brain responses between the stimulus On/Off conditions to assess the contrast-to-noise achieved in this paradigm (Fig. 3F and G). Further, repeating the block average analysis with all three hemoglobin contrasts obtainable with the HD-DOT instrument, ΔHbO_2, ΔHbR, and ΔHbT, produced both convergent maps and activation timecourses (Supplemental Fig. 3), further verifying image quality and spectroscopy performance via the ratios between the three contrasts (Zeff et al., 2007). Finally, inspection of single-subject maps (Supplemental Fig. 4) that comprise the group average indicated that the topography of the activation–bilateral responses centered on the superior temporal gyrus–was observable from a single run of the passive word listening task (i.e. 3 min of data).

3.3. Task-evoked responses with sparse array reconstruction

To evaluate the effect of reconstructing images of brain activation with a sparse array, we reconstructed images of ΔHbO_2 during passive word listening with a subset of second nearest neighbor measurements from the full set of HD-DOT measurements. Measurements were selected such that they spanned a field-of-view comparable to the HD-DOT field-of-view, but with no overlapping measurements (Fig. 4, A). A single subject's passive word listening responses for the sparse array (Fig. 4B and C) and dense array (Fig. 4, E-F) revealed an effect of measurement density on the localization of the passive word listening response in the reconstructed images.

While the sparse reconstruction reveals a pattern of bilateral activations near the superior temporal gyrus, the shape and magnitude of these responses differed from the responses reconstructed using the dense measurement array. For example, comparing the right hemisphere activations between sparse and dense reconstructions revealed that measurement density affected the spatial extent and magnitude of the reconstructed oxyhemoglobin concentration change. Importantly, these images were produced with the same underlying data—the variance between sparse and dense reconstructions cannot be attributed to variance driven by analyzing data derived from different cap fits, different imaging sessions, or different participants.

Across all participants, the dense reconstruction scheme resulted in more consistent localization of passive word listening activations across participants (Supplemental Fig. 5). While both reconstruction schemes produced group-averaged bilateral activations, greater spatial consistency was observed between individual activation maps reconstructed using a dense array of optical measurements. Additionally, individual
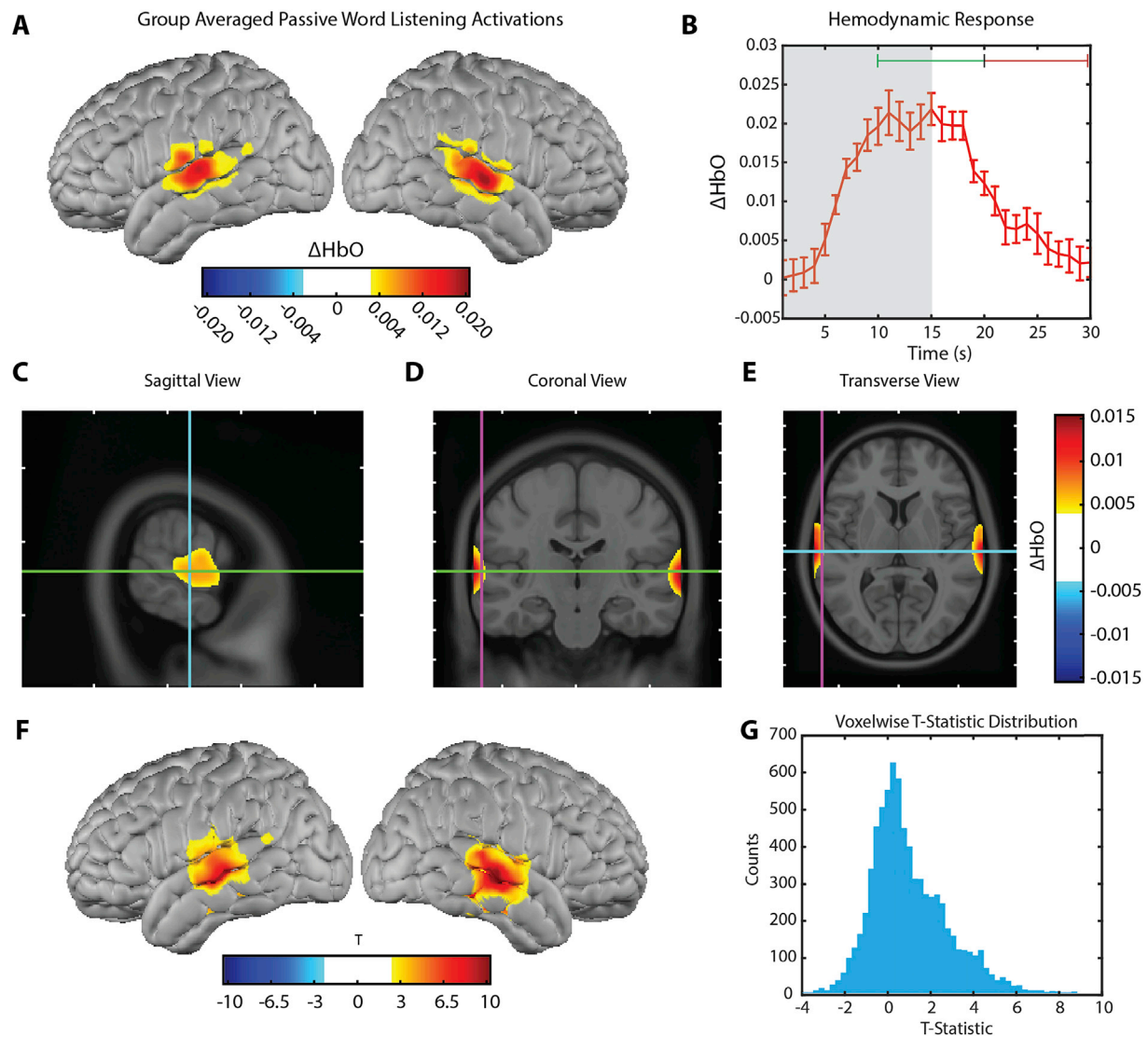
Fig. 3. Group-level passive word listening activations.
A: Block averaged oxy-hemoglobin activations associated with the passive word listening task averaged across the entire cohort of participants. Activation locations were in agreement with previously published HD-DOT results using this task, showing bilateral activations on superior temporal gyrus (Eggebrecht et al., 2014). **B:** The block averaged oxy-hemoglobin time course extracted from left superior temporal gyrus showed a stimulus-related activation. The shaded area represents the stimulation epoch, in which participants listened to concrete Spanish nouns at a rate of 1 word/second. Error bars are S.E.M. across participants. Lines across the top indicate the epochs used for block averaging: On, green line, seconds 10–19; Off, red line, seconds 20–29. **C–E:** Volumetric sagittal, coronal, and transverse views of the oxyhemoglobin activation shows depth-resolved images of the surface projection shown in **Panel A**. Crosshairs indicate the location of the voxel used to plot the timecourse displayed in **Panel B**. **F:** Random effects T map showing the contrast between "On" and "Off" stimulation periods over the participant population. **G:** Voxelwise distribution of T-statistics shown in **Panel F**.

maps reconstructed using the dense array showed greater overlap with the group-averaged activation map, further underscoring that an individual activation map reconstructed using a dense measurement array has a higher likelihood of consistently localizing the activation to the same region of superior temporal gyrus than maps reconstructed using a sparse measurement array.

3.4. Bilateral functional connectivity

We assessed bilateral, or homotopic, functional connectivity using a set of twelve seed regions (Fig. 5, A) that spanned the HD-DOT field-of-view. The seed set included seeds in superior temporal gyrus (auditory), the middle temporal lobe, visual cortex, and the temporal-parietal junction (Fig. 5, G). Seed positions were informed by prior functional connectivity analyses using HD-DOT and constrained by the present

instrument's field-of-view (Ferradal et al., 2016). The correlation matrix between seed pairs (Fig. 5, B) and individual voxelwise seed maps (Fig. 5, C–F) display the z-transformed correlation value, representing the magnitude of the correlation between a pair of oxyhemoglobin timetraces.

Bilateral connectivity is quantified through the correlation coefficient between homotopic seed pairs and is evident through elevated off-diagonal correlations in the correlation matrix (Fig. 5, B). Seed maps (Fig. 5, C–F) show the spatial extend of bilateral connectivity for four seeds with the highest homotopic connectivity, with the highest correlation values present on the ipsilateral hemisphere, near the seed region. However, areas with elevated correlations were observed in the corresponding region on the contralateral hemisphere, highlighting the capability of the field HD-DOT instrument to sample connectivity in multiple, distributed regions throughout the field-of-view.
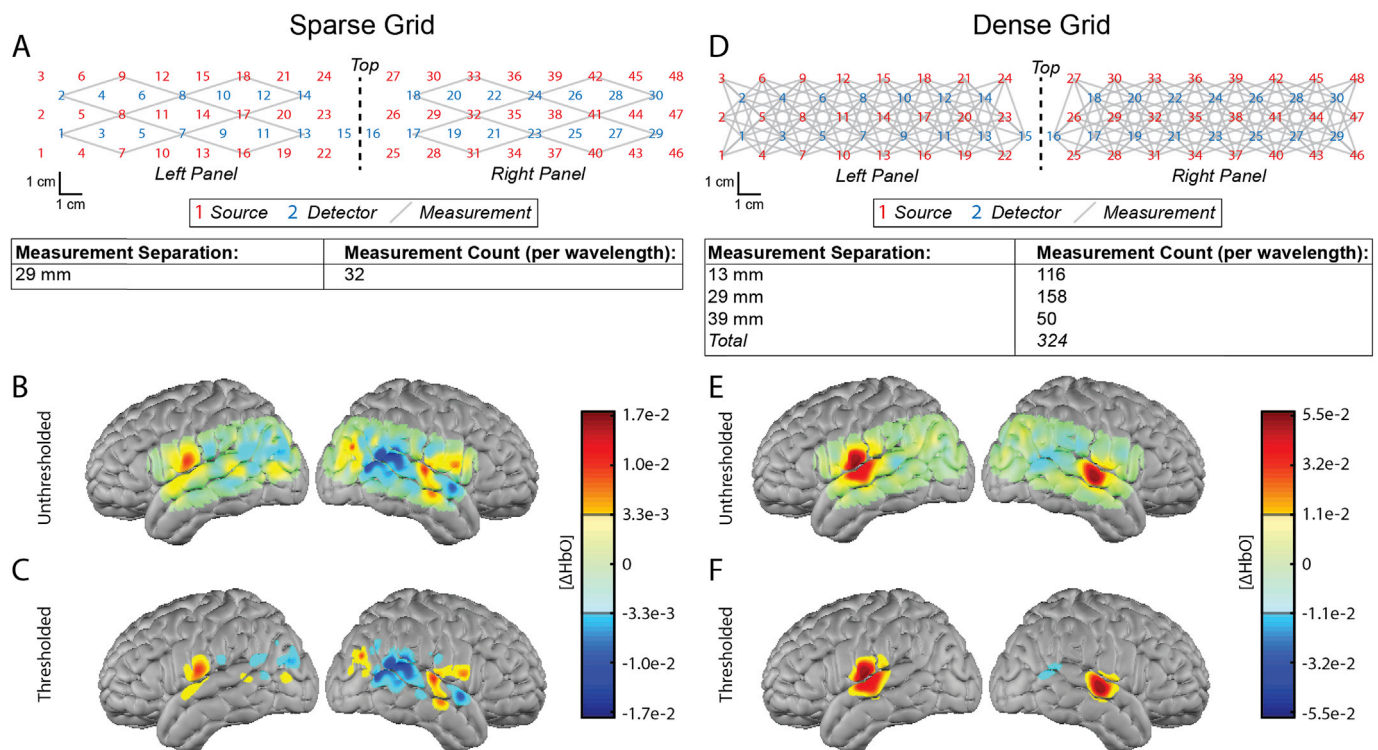
Sparse Grid

A: [grid with sources and detectors]

Measurement Separation:	Measurement Count (per wavelength):
29 mm	32

1 Source 2 Detector / Measurement

Dense Grid

D: [dense grid with sources and detectors]

Measurement Separation:	Measurement Count (per wavelength):
13 mm	116
29 mm	158
39 mm	50
Total	324

1 Source 2 Detector / Measurement

Fig. 4. Sparse and dense HD-DOT image reconstruction.
A: The sparse measurement grid used to reconstruct tomographic images of brain function using a measurement count more typical of field-based fNIRS instruments. Sources (red) and detectors (blue) show optode locations in the full HD-DOT optode array. The subset of HD-DOT measurements used to reconstruct sparse-measurement fNIRS images are indicated by grey lines. All 32 measurements were at a single source-detector separation of 29 mm. **B:** Unthresholded oxy-hemoglobin activations reconstructed using sparse measurements obtained during the passive word listening task. **C:** Thresholded image of data shown in **Panel B. D:** The full HD-DOT optode array includes 324 measurements at 3 source-detector separations, which were subsequently used for tomographic image reconstruction of the same data shown in **Panels B, C. E:** Unthresholded oxy-hemoglobin activations reconstructed using dense measurements obtained during the passive word listening task (i.e. the same data used for sparse reconstruction). **F:** Thresholded image of data shown in **Panel E**.

4. Discussion

High-density diffuse optical tomography instruments use a large channel count and dense, overlapping optical measurements to produce fMRI-comparable images of cortical hemodynamics during tasks and rest (Eggebrecht et al., 2012, 2014; Ferradal et al., 2016). In this work, we extended the use of HD-DOT to the new application of imaging brain function in a cohort of malnourished children in Cali, Colombia. Imaging this population was feasible due to the utilization of a mobile and wearable optical neuroimaging modality, as low-resource settings demand imaging tools that can function in the absence of expensive, dedicated immobile infrastructure (Lloyd-Fox et al., 2014, 2016; Roberts et al., 2017). Here, HD-DOT was used to measure task-evoked responses and homotopic functional connectivity in Cali, Colombia, establishing the capability of measuring spatially distributed brain function in a portable HD-DOT instrument.

Like other work introducing field imaging instruments in novel settings, the focus of the imaging performed in this work was to obtain maps of brain function in good agreement with previously published HD-DOT results, rather than investigating potential group-level differences between typically-developing and malnourished children (Lloyd-Fox et al., 2014). Indeed, the images obtained with the HD-DOT instrument introduced in this work agreed with previous HD-DOT investigations performed with other instruments, across multiple sites, in both healthy adults and infants (Eggebrecht et al., 2014; Ferradal et al., 2016). This finding indicated that the mobile HD-DOT implementation reported, including instrument design, channel count, and optode configuration, noise censoring and movie viewing protocol successfully managed to retain much of the data quality previously shown in healthy adults.

Importantly, the instrument's field-of-view constrains the available experimental questions. In this work, the field-of-view based on prior instruments, and slightly expanded relative to these instruments, due to the availability of additional source-detector channels (Ferradal et al., 2016). Future work, using instruments with expanded channel counts and a larger field-of-view, would permit exploration of additional functional systems in this experimental population beyond the auditory stimulation protocol used in this work. The ergonomic challenges posed by adding fibers to increase the HD-DOT field-of-view can be managed using detection methods that support lightweight fibers (e.g. sCMOS cameras) (Bergonzi et al., 2018). Furthermore, while this work utilized a block design to present the auditory word stimuli, future work can also incorporate event-related designs to minimize the predictability of the stimulus timing.

The sensitivity to homotopic functional connectivity established in this analysis sets the stage for using this powerfully predictive measurement in future analyses that are more targeted at identifying correlates of malnutrition burden (Estep et al., 2014; Smyser et al., 2011, 2013). Prior work using fetal and infant fMRI demonstrates the emergence of bilateral functional connectivity over development, highlighting the utility of this measure in future assessments of a child's developmental status. Importantly, the functional connectivity scans collected in this work were during passive movie viewing conditions. While this condition means that functional connectivity results from this work may not be directly comparable to results obtained during rest (i.e. passive fixation), movie viewing is a powerful tool to enhance subject compliance during functional connectivity scans and reduce the pernicious effects of head motion (Greene et al., 2018; Vanderwal et al., 2015, 2018). While seed-based connectivity analysis were used herein to establish
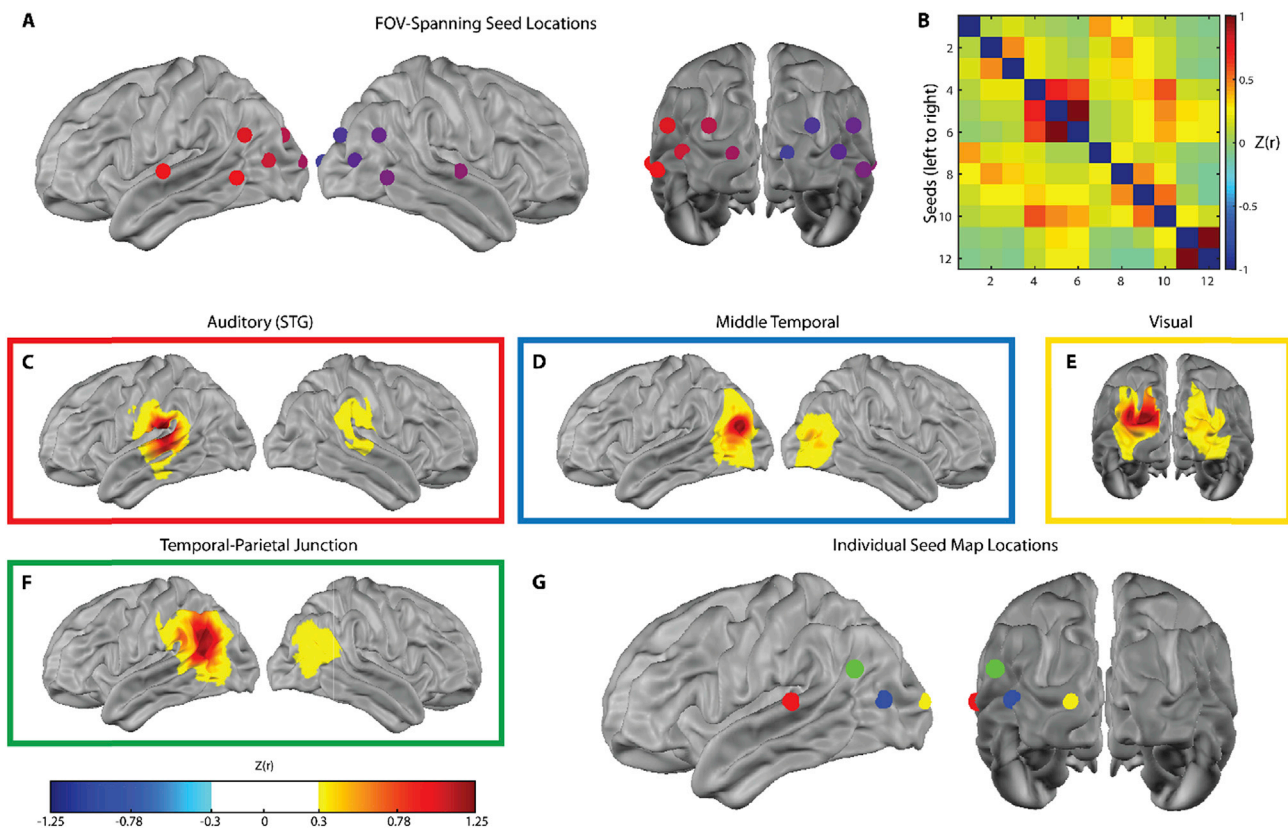
Fig. 5. Homotopic functional connectivity.
Homotopic functional connectivity was assessed using a seed-based approach. **A:** Location of the 12 seeds spanning the HD-DOT field-of-view used in the functional connectivity analysis. **B:** Correlation matrix displaying the Fisher z-transformed correlation magnitudes for pairwise seed correlations. **C–F:** Seed maps showing z-transformed correlation coefficients for four of the seeds with the strongest bilateral connectivity. Seed maps were generated by computing the Pearson correlation between the Pearson correlation between the oxy-hemoglobin timeseries extracted from the 5-mm radius spherical seed and every voxel in the field of view. **G:** Seed locations for the seed maps shown in **Panels C–F**; the colors of the seed map outlines correspond to the color of the seed.

proof of principle for the novel field setting and followed prior work using HD-DOT to assess functional connectivity (Ferradal et al., 2016), future work can leverage more sophisticated analyses to better elucidate the brain's functional network architecture (e.g. ICA (Smith et al., 2011), voxel-wise and measurement-wise parcellation (Yeo et al., 2011; Power et al., 2011), and boundary mapping analyses (Eggebrecht et al., 2014)) and its relationship to behavior (Eggebrecht et al., 2017; Marrus et al., 2018), development (Marek et al., 2019; Wheelock et al., 2019), exposure (Thomason et al., 2019), and outcome (Wheelock et al., 2018; Tooley et al., 1093).

Future analyses with this dataset may leverage the rich, multimodal content of the movie stimulus by filtering the data to a band more appropriate for measuring task-evoked responses (e.g. $0.02 < f < 0.5$ Hz). Evaluating the task-evoked responses during movie viewing opens additional analytic possibilities, including assessing synchronized brain responses during passive movie viewing (Hasson et al., 2004; Fishell et al., 2019). Critically, prior work using fMRI has shown that the extent to which an individual exhibits synchronized brain responses during passive movie viewing is related to mathematical and linguistic ability, and also varies between typical and atypical development (Cantlon and Li, 2013; Moraczewski et al., 2018; Byrge et al., 2015). Consequently, this study establishes a foundation for incorporating these powerful analyses in ongoing assessments of developmental status and malnutrition burden.

A key difference between the HD-DOT system introduced in this work and other fNIRS systems is the density of optical measurements. The system introduced in this work provides coverage of both hemispheres, using a total of 78 optodes, resulting in up to 324

measurements per wavelength and enabling tomographic image reconstruction. In contrast, fNIRS systems often have an order of magnitude fewer measurements and/or limited cortical coverage; consequently, topographic analysis of brain function is often favored over analyzing tomographically reconstructed images (Lloyd-Fox et al., 2014; Everdell et al., 2005). In this work, we directly compared tomographically reconstructed images using both sparse and dense measurement configurations. While both configurations detected a hemodynamic signal change associated with stimulus presentation, the localization of the resulting signal change varied as a function of grid density, with consistently localized brain activations most prominently evident in the dense reconstructions. Accordingly, an instrument's channel count is a critical consideration in experiments demanding both detection and localization of brain activations.

While prior work with simulations and *in-vivo* comparisons of grid density show that increasing grid density improves image quality characteristics including the system's point-spread function and localization error (White and Culver, 2010b; Habermehl et al., 2012; Tian et al., 2009; Yamamoto et al., 2002), one key limitation of the sparse and dense measurement comparison presented here is the lack of a "ground truth" image for evaluating the quality of the two reconstruction schemes used in this work. Consequently, follow-up work will require comparing the images resulting from sparse and dense image reconstruction schemes using subject-matched images obtained using a reference modality, such as fMRI. Additionally, this follow-up work should consider the role of different superficial signal regression techniques (e.g. average of the global signal versus average of a short measurement pair) on the comparability of tomographically reconstructed DOT images to fMRI

reference images (Burns-Yocum et al., 2018).

In addition to the imaging results presented in this work, our results highlight the usability of the HD-DOT instrument in non-laboratory contexts. After four hours of setup, the HD-DOT instrument was ready for imaging, and posed no infrastructure requirements beyond electricity. New users learned to perform cap fit and data collection procedures within a week of supervised imaging. This manageable learning curve is a significant advantage of optical neuroimaging instruments relative to other imaging modalities (e.g. MRI), and is likely a contributing factor to the burgeoning use of fNIRS and HD-DOT instruments in the field. Other instruments, such as EEG, have widespread use and also offer exceptional portability, but still require end-users to be trained on cap positioning and data acquisition. Ultimately, the experimental question at hand, considered alongside the signal origins, localization capabilities, and setup efforts associated with the available neuroimaging tools will allow experimenters to select the most appropriate imaging modality. While HD-DOT and fNIRS are a less mature technology than EEG, recently significant progress has been made towards standardizing data collection, pre-processing, motion artifact detection and mitigation, image reconstruction, anatomical registration, and analysis pipelines with multiple toolboxes available (e.g., Homer (Di Lorenzo et al., 2019), NIRS Brain AnalyzIR Toolbox (Santosa et al., 2019), NeuroDOT (Eggebrecht et al., 2014), NIRS-SPM (Ye et al., 2009). As these efforts continue, it is reasonable to expect that the barriers to use will lower, approaching these of EEG.

Optical methods have been used globally to perform neuromonitoring and neuroimaging assessments in settings that would not be reachable with imaging modalities that require dedicated infrastructure. fNIRS and DCS-based studies of childhood malnutrition have assayed various aspects of brain function hypothesized to be impacted by malnutrition in the first 1000 days of life, including executive functioning and social processing (Lloyd-Fox et al., 2014, 2016; Lloyd-Fox et al., 2019; Roberts et al., 2017). These studies incorporate cross-culturally appropriate, risk sensitive imaging paradigms to provide insight into malnutrition-related deviances in developmental trajectories (Lloyd-Fox et al., 2019). While these studies focused on younger participants (i.e. < 2 years), continued investigation of the older children in the present cohort will provide complementary insight into the effects of long-term malnutrition over the course of childhood.

5. Conclusions

The present work establishes HD-DOT as an optical neuroimaging modality suitable for investigations of brain function in low-resource contexts that demand mobile instruments, while maintaining cortical coverage and image resolution associated with less portable modalities. Reconstructing subject-matched simultaneous data with fewer measurements revealed that optical measurement density is a contributing factor in reconstructing consistently localized brain activations. Finally, the combination of task-evoked and functional connectivity maps evaluated in this work provide a requisite foundation for targeted investigations of the developing brain in the context of childhood malnutrition, including identifying and characterizing a child's risk to foster future intervention development (Raizada and Kishiyama, 2010).

The data quality report generated during image reconstruction indicates the measurement quality obtained during a single scan and includes multiple measurement quality assessments used to determine the usability of a scan in real-time. This report was generated from a representative subject during a passive word listening acquisition. **A:** The average light level for first nearest neighbor (NN1) measurements across the two panels of the HD-DOT cap indicated relatively strong light levels across the cap. **B:** A plot of light level as a function of source-detector separation (i.e. measurement distance) showed log-linear light falloff, as would be expected in biological tissue. **C:** The plot of measurement retention for this acquisition showed

measurements retained for subsequent image reconstruction (green lines), as well as optodes where at least 33% of measurements were rejected (black circles). In this cap fit, 232/232 NN1, 295/316 NN2, and 27/100 NN3 measurements were retained. **D:** The histogram of measurement-wise temporal variance indicated that most measurements are below the temporal variance threshold (7.5%, red line) imposed to exclude measurements contaminated by movement or poor optode coupling. **E:** The pulse signal-to-noise for first nearest-neighbor measurements showed, in general, strong signal-to-noise ratio at the participant's pulse frequency, indicating good sensitivity to vascular physiology needed to image cortical hemodynamics. **F:** A plot of individual second nearest-neighbor measurements showed sensitivity to the participant's pulse, and a lack of global variance across measurements that could be associated with global noise introduced by head motion. (For interpretation of the references to color in this figure legend, the reader is referred to the Web version of this article.)

Data availability

The data and analysis tools used in this study are available upon reasonable request to the corresponding author.

Author contributions

JPC, ATE, CDS, AMA, and AKF designed the experiments. AMA established the imaging site in Cali, Colombia and the infrastructure needed for participant recruitment. CPV and AKF collected imaging data. AKF developed analysis code under the supervision of JPC. CPV and AKF reconstructed and analyzed HD-DOT data. JPC, ATE, and EJR designed HD-DOT instrumentation. EJR and AKF built the HD-DOT instrument and cap. EJR assembled and characterized the HD-DOT instrument in Cali, Colombia, with assistance from CPV, AMA, and AKF. MT and AMA performed physical examinations of participants in Colombia. ATE and TMB designed the sparse/dense measurement reconstruction analysis. AS developed data quality metrics under the supervision of JPC and ATE. AKF wrote the manuscript under the supervision of JPC, with input from all authors.

Declaration of competing interest

The authors declare no conflicting interests, financial or otherwise.

Appendix A. Supplementary data

Supplementary data to this article can be found online at https://doi.org/10.1016/j.neuroimage.2020.116541.

References

Barrett, D.E., Radke-Yarrow, M., Klein, R.E., 1982. Chronic malnutrition and child behavior: effects of early caloric supplementation on social and emotional functioning at school age. Dev. Psychol. 18, 541–556.

Bergonzi, K.M., et al., 2018. Lightweight sCMOS-based high-density diffuse optical tomography. NPh 5, 035006.

Bevilacqua, F., et al., 1999. In vivo local determination of tissue optical properties: applications to human brain. Appl. Optic. 38, 4939–4950.

Black, M.M., et al., 2019. Mechanisms linking height to early child development among infants and preschoolers in rural India. Dev. Sci., e12806 https://doi.org/10.1111/desc.12806.

Bluestone, A., Abdoulaev, G., Schmitz, C., Barbour, R., Hielscher, A., 2001. Three-dimensional optical tomography of hemodynamics in the human head. Optic Express 9, 272–286.

Burns-Yocum, T.M., et al., 2018. Quantitative assessment of image quality of sparse functional near infrared spectroscopy vs high-density diffuse optical tomography. *paper* JTh3A.55 JTh3A.55. In: Biophotonics Congress: Biomedical Optics Congress 2018 (Microscopy/Translational/Brain/OTS). Optical Society of America. https://doi.org/10.1364/TRANSLATIONAL.2018.JTh3A.55, 2018.

Byrge, L., Dubois, J., Tyszka, J.M., Adolphs, R., Kennedy, D.P., 2015. Idiosyncratic brain activation patterns are associated with poor social comprehension in autism. J. Neurosci. 35, 5837–5850.

Cantlon, J.F., Li, R., 2013. Neural activity during natural viewing of Sesame street statistically predicts test scores in early childhood. PLoS Biol. 11, e1001462.

Chugani, H.T., Phelps, M.E., Mazziotta, J.C., 1987. Positron emission tomography study of human brain functional development. Ann. Neurol. 22, 487–497.

Cusick, S.E., Georgieff, M.K., 2012. Nutrient supplementation and neurodevelopment: timing is the key. Arch. Pediatr. Adolesc. Med. 166, 481–482.

Custo, A., Wells, W.M., Barnett, A.H., Hillman, E.M.C., Boas, D.A., 2006. Effective scattering coefficient of the cerebral spinal fluid in adult head models for diffuse optical imaging. Appl. Optic. 45, 4747–4755.

Dehghani, H., et al., 2008. Near infrared optical tomography using NIRFAST: algorithm for numerical model and image reconstruction. Commun. Numer. Methods Eng. 25, 711–732.

Di Lorenzo, R., et al., 2019. Recommendations for motion correction of infant fNIRS data applicable to multiple data sets and acquisition systems. Neuroimage 200, 511–527.

Eggebrecht, A.T., et al., 2012. A quantitative spatial comparison of high-density diffuse optical tomography and fMRI cortical mapping. Neuroimage 61, 1120–1128.

Eggebrecht, A.T., et al., 2014. Mapping distributed brain function and networks with diffuse optical tomography. Nat. Photon. 8, 448–454.

Eggebrecht, A.T., et al., 2017. Joint attention and brain functional connectivity in infants and toddlers. Cerebr. Cortex 27, 1709–1720.

Estep, M.E., et al., 2014. Diffusion tractography and neuromotor outcome in very preterm children with white matter abnormalities. Pediatr. Res. 76, 86–92.

Everdell, N.L., et al., 2005. A frequency multiplexed near-infrared topography system for imaging functional activation in the brain. Rev. Sci. Instrum. 76, 093705.

Ferradal, S.L., Eggebrecht, A.T., Hassanpour, M., Snyder, A.Z., Culver, J.P., 2014. Atlas-based head modeling and spatial normalization for high-density diffuse optical tomography: in vivo validation against fMRI. Neuroimage 85 (Pt 1), 117–126.

Ferradal, S.L., et al., 2016. Functional imaging of the developing brain at the bedside using diffuse optical tomography. Cerebr. Cortex 26, 1558–1568.

Fishell, A.K., Burns-Yocum, T.M., Bergonzi, K., Eggebrecht, A.T., Culver, J.P., 2019. Mapping brain function during naturalistic viewing using high-density diffuse optical tomography. Sci. Rep. 9, 11115.

Fonov, V., et al., 2011. Unbiased average age-appropriate atlases for pediatric studies. Neuroimage 54, 313–327.

Goyal, M.S., Raichle, M.E., 2013. Gene expression-based modeling of human cortical synaptic density. Proc. Natl. Acad. Sci. Unit. States Am. 110, 6571–6576.

Goyal, M.S., Hawrylycz, M., Miller, J.A., Snyder, A.Z., Raichle, M.E., 2014. Aerobic glycolysis in the human brain is associated with development and neotenous gene expression. Cell Metabol. 19, 49–57.

Grantham-McGregor, S.M., Powell, C.A., Walker, S.P., Himes, J.H., 1991. Nutritional supplementation, psychosocial stimulation, and mental development of stunted children: the Jamaican Study. Lancet 338, 1–5.

Grantham-McGregor, S., et al., 2007. Developmental potential in the first 5 years for children in developing countries. Lancet 369, 60–70.

Greene, D.J., et al., 2016. Multivariate pattern classification of pediatric Tourette syndrome using functional connectivity MRI. Dev. Sci. 19, 581–598.

Greene, D.J., et al., 2018. Behavioral interventions for reducing head motion during MRI scans in children. Neuroimage 171, 234–245.

Gregg, N.M., White, B.R., Zeff, B.W., Berger, A.J., Culver, J.P., 2010. Brain specificity of diffuse optical imaging: improvements from superficial signal regression and tomography. Front. Neuroenergetics 2.

Habermehl, C., et al., 2012. Somatosensory activation of two fingers can be discriminated with ultrahigh-density diffuse optical tomography. Neuroimage 59, 3201–3211.

Hasson, U., Nir, Y., Levy, I., Fuhrmann, G., Malach, R., 2004. Intersubject synchronization of cortical activity during natural vision. Science 303, 1634–1640.

Hoddinott, J., Maluccio, J.A., Behrman, J.R., Flores, R., Martorell, R., 2008. Effect of a nutrition intervention during early childhood on economic productivity in Guatemalan adults. Lancet 371, 411–416.

Iannotti, L., et al., 2016. Nutrition factors predict earlier acquisition of motor and language milestones among young children in Haiti. Acta Paediatr. 105, e406–411.

Jensen, S.K.G., et al., 2019. Neural correlates of early adversity among Bangladeshi infants. Sci. Rep. 9, 3507.

JL, G.J., R. Structural MRI of pediatric brain development: what have we learned and where are we going? - PubMed - NCBI. Available at: https://www.ncbi.nlm.nih.gov/pubmed/20826305 (Accessed: 31st March 2019).

Joseph, D.K., Huppert, T.J., Franceschini, M.A., Boas, D.A., 2006. Diffuse optical tomography system to image brain activation with improved spatial resolution and validation with functional magnetic resonance imaging. Appl. Opt., AO 45, 8142–8151.

Kuzawa, C.W., et al., 2014. Metabolic costs and evolutionary implications of human brain development. Proc. Natl. Acad. Sci. U. S. A. 111, 13010–13015.

Liu, J., Raine, A., Venables, P.H., Dalais, C., Mednick, S.A., 2003. Malnutrition at age 3 years and lower cognitive ability at age 11 years: independence from psychosocial adversity. Arch. Pediatr. Adolesc. Med. 157, 593–600.

Lloyd-Fox, S., et al., 2014. Functional near infrared spectroscopy (fNIRS) to assess cognitive function in infants in rural Africa. Sci. Rep. 4, 4740.

Lloyd-Fox, S., et al., 2016. fNIRS in Africa & Asia: an objective measure of cognitive development for global health settings. Faseb. J. 30, 1149.18-1141149.18.

Lloyd-Fox, S., et al., 2019. Habituation and novelty detection fNIRS brain responses in 5- and 8-month-old infants: the Gambia and UK. Dev. Sci., e12817, 0.

Marek, S., et al., 2019. Identifying reproducible individual differences in childhood functional brain networks: an ABCD study. Dev. Cognit. Neurosci. 40, 100706.

Marrus, N., et al., 2018. Walking, gross motor development, and brain functional connectivity in infants and toddlers. Cerebr. Cortex 28, 750–763.

Martorell, R., 1999. The nature of child malnutrition and its long-term implications. Food Nutr. Bull. 20, 288–292.

Martorell, R., et al., 2010. Weight gain in the first two years of life is an important predictor of schooling outcomes in pooled analyses from five birth cohorts from low- and middle-income countries. J. Nutr. 140, 348–354.

Mazziotta, J., et al., 2001. A probabilistic atlas and reference system for the human brain: international Consortium for Brain Mapping (ICBM). Philos. Trans. R. Soc. Lond. B Biol. Sci. 356, 1293–1322.

McKay, H., Sinisterra, L., McKay, A., Gomez, H., Lloreda, P., 1978. Improving cognitive ability in chronically deprived children. Science 200, 270–278.

Moraczewski, D., Chen, G., Redcay, E., 2018. Inter-subject synchrony as an index of functional specialization in early childhood. Sci. Rep. 8, 2252.

Murthy, K.D., Desiraju, T., 1991. Synapses in developing cingulate and hippocampal cortices in undernourished rats. Neuroreport 2, 433–436.

Nelson, C.A., 2015. An international approach to research on brain development. Trends Cognit. Sci. 19, 424–426.

Power, J.D., et al., 2011. Functional network organization of the human brain. Neuron 72, 665–678.

Prado, E.L., Dewey, K.G., 2014. Nutrition and brain development in early life. Nutr. Rev. 72, 267–284.

Raizada, R.D.S., Kishiyama, M.M., 2010. Effects of socioeconomic status on brain development, and how cognitive neuroscience may contribute to levelling the playing field. Front. Hum. Neurosci. 4.

Roberts, S.B., et al., 2017. A pilot randomized controlled trial of a new supplementary food designed to enhance cognitive performance during prevention and treatment of malnutrition in childhood. Curr Dev Nutr 1.

Santosa, H., Fishburn, F., Zhai, X., Huppert, T.J., 2019. Investigation of the sensitivity-specificity of canonical- and deconvolution-based linear models in evoked functional near-infrared spectroscopy. NPh 6, 025009.

Sherafati, A., Eggebrecht, A.T., Burns-Yocum, T.M., Culver, J.P., 2017. A global metric to detect motion artifacts in optical neuroimaging data (Conference Presentation). In: Neural Imaging and Sensing, 10051. International Society for Optics and Photonics, p. 1005112.

Smith, S.M., et al., 2011. Network modelling methods for FMRI. Neuroimage 54, 875–891.

Smyser, C.D., et al., 2010. Longitudinal analysis of neural network development in preterm infants. Cerebr. Cortex 20, 2852–2862.

Smyser, C.D., Snyder, A.Z., Neil, J.J., 2011. Functional connectivity MRI in infants: exploration of the functional organization of the developing brain. Neuroimage 56, 1437–1452.

Smyser, C.D., et al., 2013. Effects of white matter injury on resting state fMRI measures in prematurely born infants. PloS One 8, e68098.

Strangman, G., Culver, J.P., Thompson, J.H., Boas, D.A., 2002. A quantitative comparison of simultaneous BOLD fMRI and NIRS recordings during functional brain activation. Neuroimage 17, 719–731.

Thomason, M.E., et al., 2019. Prenatal lead exposure impacts cross-hemispheric and long-range connectivity in the human fetal brain. Neuroimage 191, 186–192.

Thompson, R.A., Nelson, C.A., 2001. Developmental science and the media. Early brain development. Am. Psychol. 56, 5–15.

Tian, F., Alexandrakis, G., Liu, H., 2009. Optimization of probe geometry for diffuse optical brain imaging based on measurement density and distribution. Appl. Opt., AO 48, 2496–2504.

Tooley, U. A. et al. Associations between neighborhood SES and functional brain network development. Cerebr. Cortex doi:10.1093/cercor/bhz066.

Vanderwal, T., Kelly, C., Eilbott, J., Mayes, L.C., Castellanos, F. X. Inscapes, 2015. A movie paradigm to improve compliance in functional magnetic resonance imaging. Neuroimage 122, 222–232.

Vanderwal, T., Eilbott, J., Castellanos, F.X., 2018. Movies in the magnet: naturalistic paradigms in developmental functional neuroimaging. Dev. Cognit. Neurosci. https://doi.org/10.1016/j.dcn.2018.10.004.

Waber, D.P., et al., 2011. Cognitive impairment as a mediator in the developmental pathway from infant malnutrition to adolescent depressive symptoms in Barbadian youth. J. Dev. Behav. Pediatr. 32, 225–232.

Wheelock, M.D., et al., 2018. Altered functional network connectivity relates to motor development in children born very preterm. Neuroimage 183, 574–583.

Wheelock, M.D., et al., 2019. Sex differences in functional connectivity during fetal brain development. Dev. Cognit. Neurosci. 36, 100632.

White, B.R., Culver, J.P., 2010. Phase-encoded retinotopy as an evaluation of diffuse optical neuroimaging. Neuroimage 49, 568–577.

White, B.R., Culver, J.P., 2010. Quantitative evaluation of high-density diffuse optical tomography: in vivo resolution and mapping performance. JBO 15, 026006.

Wiggins, R.C., 1982. Myelin development and nutritional insufficiency. Brain Res. 257, 151–175.

Yamamoto, T., et al., 2002. Arranging optical fibres for the spatial resolution improvement of topographical images. Phys. Med. Biol. 47, 3429–3440.

Ye, J.C., Tak, S., Jang, K.E., Jung, J., Jang, J., 2009. NIRS-SPM: statistical parametric mapping for near-infrared spectroscopy. Neuroimage 44, 428–447.

Yeo, B.T.T., et al., 2011. The organization of the human cerebral cortex estimated by intrinsic functional connectivity. J. Neurophysiol. 106, 1125–1165.

Zeff, B.W., White, B.R., Dehghani, H., Schlaggar, B.L., Culver, J.P., 2007. Retinotopic mapping of adult human visual cortex with high-density diffuse optical tomography. Proc. Natl. Acad. Sci. U.S.A. 104, 12169–12174.